Limitations and considerations for electrical resistivity and induced polarization imaging of riverbed sediments: Observations from laboratory, field, and synthetic experiments.

P. McLachlan[1], J. Chambers[2], S. Uhlemann[3], A. Binley[1]

1 – Lancaster Environmental Centre, Lancaster University, LA1 4YQ, UK

2 – Geophysical Tomography Team, British Geological Survey, Keyworth, NG12 5GG, UK

3 – Lawrence Berkeley National Laboratory, Berkeley, CA 94720, US

Corresponding author email address – p.mclachlan@outook.com

Abstract

Characterization of riverbed sediments is important for understanding groundwater (GW) and surface water (SW) interactions, and their consequent implications for ecological and environmental health. There have been numerous studies using geoelectrical methods for GW-SW interaction studies; however, most applications have not focused on obtaining quantitative information. For instance, although numerous laboratory studies highlight the relationship between geoelectrical properties and relevant parameters (e.g. specific surface area, hydraulic conductivity, and cation exchange capacity), such relationships are not commonly applied to field-scale studies. Furthermore, in addition to the spatial resolution obstacles typically present when applying petrophysical models to field data, geoelectrical data from aquatic environments have additional complications arising from the presence of a conductive water column overlying a resistive bed. Inadequate consideration of these complications may further preclude the reliable use of such petrophysical models. In this work, laboratory measurements, synthetic modeling, and field measurements were conducted in a third-order river where the riverbed comprises alluvial gravel and underlying red sand. A strong relationship (R^2 = 0.72) between imaginary conductivity and specific surface area was observed, and laboratory results were comparable to previous studies. It was demonstrated through synthetic modeling that river stage and channel width, regularization across the river-riverbed interface, and incorrect constraints of both the river conductivity and river stage can have varying influence on inverted geoelectrical images. Reliable geoelectrical images require *a priori* definition of river stage and conductivity, however inversion constraints using incorrect *a priori* values result in misleading artifacts. The conductivity image obtained from the field data in this work appeared to reflect the geoelectrical structure anticipated from the laboratory data; however, the phase angle image did not. Application of the petrophysical model to field data resulted in a model of the riverbed comprising three-layers, however, given the prevalence of

artifacts in aquatic applications caution is required when making interpretations. Although this study focused on riverbed characterization, findings here demonstrate common pitfalls of inversion of aquatic-based geoelectrical data. Primarily, they highlight that synthetic modeling ought to be used to alleviate any uncertainty in the interpretation of geoelectrical models before predictions about GW-SW interactions can be made.

1. Introduction

Riverbed sediments play an active role in solute transfer between groundwater (GW) and surface water (SW); consequently, they have implications for catchment-scale ecological health. Zones where GW and SW mix are of interest as they are characterized by unique biogeochemical conditions that permit the transformation of nutrients and pollutants (Harvey and Gooseff, 2015). Properties of riverbeds such as specific surface area, cation exchange capacity (CEC), and hydraulic conductivity are important to characterize as they influence residence times of nutrients and pollutants, and the potential for their biogeochemical transformation. For instance, sediments with a large specific surface area and high CEC values have a higher potential for attenuation of nutrients and pollutants (Harvey and Fuller, 1998). Furthermore, the significance of such riverbed parameters has been recognized for several decades (e.g. Bencala et al., 1984; Triska et al., 1993; Lansdown et al., 2015).

In the past 15 years, there has been numerous electrical resistivity imaging (ERI) and induced polarization (IP) applications to target properties relevant to GW-SW interactions (see review by McLachlan et al., 2017). For example, ERI methods have been used to reveal the extent of the hyporheic zone (e.g. Ward et al. 2010; Toran et al., 2013), characterize the underlying structure of rivers and lakes (e.g. Clifford and Binley, 2010; Crook et al., 2008; Colombero et al., 2014), and locate zones of GW up-welling (e.g. Mitchell et al., 2008; Gagliano et al., 2009). Additionally, IP methods have been used to characterize structure (e.g. Slater et al., 2010) and hydraulic conductivity (Benoit et al., 2019). There has also been substantial laboratory work using spectral IP (SIP) methods whereby electrical conductivity and phase angle are measured across broad frequency ranges, e.g. from 1 mHz to 1000 Hz. Much of this work has demonstrated the sensitivity of SIP to specific surface area, often expressed as pore normalized surface area (S_{por}), hydraulic conductivity, and CEC (e.g. Slater, 2007; Leroy, 2009; Revil, 2012). Despite these concurrent applications, there have been limited studies where laboratory-derived petrophysical relationships are used to interpret field data in GW-SW interaction studies (e.g. Slater et al., 2010).

Aquatic applications of ERI and IP are more challenging than terrestrial applications due to the presence of a conductive water column overlying a more resistive bed. Several publications have

addressed issues associated with aquatic ERI surveys and their sensitivity, e.g. Snyder et al. (2002), Day-Lewis et al. (2006), Orlando (2013). For instance, although floating arrays are more efficient in towed surveys, they have poorer investigation depths than submerged arrays (Day-Lewis et al., 2006) and whilst bottom-towed arrays have been used to improve investigation depth (e.g. Wynn 1988; Kelly et al., 2009); equipment can become snagged on rough bedforms or vegetation. Consequently, most studies using submerged arrays have adopted fixed (anchored) arrays; this has the added benefit that reciprocal measurements can be obtained to allow for appropriate data weighting in inverse modeling. Additionally, although studies have used different materials for electrodes, e.g. graphite (Slater et al., 2010) or lead (e.g. Clifford and Binley, 2010), most aquatic electrical imaging work has used stainless-steel electrodes (e.g. Ward et al., 2010; Benoit et al., 2019).

Several authors have also explored the reliability of inversion of aquatic data, such as the effect of the erroneous constraint of water column properties has on ERI inversions (e.g. Day-Lewis et al., 2006). Because the conductivity and stage of aquatic bodies can often be measured conveniently, e.g. stage can be measured using meter sticks or acoustic sensors; it can be supplied as *a priori* knowledge to inversions to improve the reliability of the results. Although the inclusion of such knowledge has been investigated for ERI using synthetic studies, similar studies have not been conducted for IP, and the rationale behind, or details of, inversion decisions are often not discussed in aquatic ERI and IP applications.

The principal aim of this work is to determine if relationships derived in the laboratory could be applied to the field and to understand the limitations of aquatic IP imaging. This included laboratory-based SIP, specific surface area, and CEC measurements of intrusively obtained riverbed samples, several synthetic modeling cases, and collection and inversion of field IP data. Specifically, synthetic modeling cases were used to investigate: (1) the sensitivity of geoelectrical measurements to the riverbed and the riverbank; (2) the influence of constraining river properties on the inversion process, and (3) the influence of errors in both geoelectrical data and measurements of river properties on the inversion process. In doing so challenges and limitations of ERI and IP in aquatic environments were explored and several important considerations for future work were highlighted. Within the study, geoelectrical properties are represented in terms of complex conductivity: real electrical conductivity, σ'; quadrature (or imaginary) electrical conductivity, σ"; and phase angle, φ. The convention of positive phase angles, to signify polarization (positive IP effect), is used throughout.

2. Materials and methods

96 2.1. Study site

97 Fieldwork was conducted on the River Leith; see Fig. 1, a tributary of the River Eden (Cumbria, UK).
98 The River Eden catchment is a fault-bound basin 50 km long and 5 to 15 km wide with Permian and
99 Triassic sandstone bedrock (Allen et al., 2010). The catchment contains extensive Quaternary
100 deposits comprising till, glacial-fluvial out-wash, and alluvial deposits. Much of the work conducted
101 at the field site, and across the catchment, has been concerned with the direction of GW flow paths
102 and biogeochemical processes occurring at the GW-SW interface concerning river loading of legacy
103 nitrate from agriculture (Heppell et al., 2014; Lansdown et al., 2015).

104 At the field site, the riverbed comprises a mixture of alluvial pebbles, gravels, and sands overlying
105 unconsolidated red sands and silts, all underlain by the Penrith Sandstone aquifer (Allen et al., 2010).
106 The riverbed is characterized by a series of riffle and pool sequences, and is predominantly GW fed;
107 however, Käser et al. (2009) indicated the potential for SW down-welling at the site during storm
108 events which was later confirmed experimentally by Dudley-Southern and Binley (2015). Most of the
109 studies have focused on nitrate loading from the GW (e.g. Krause et al., 2009; Lansdown et al., 2012;
110 2015; Heppell et al., 2014). These studies have revealed evidence of heterogeneity in redox
111 processes controlling nitrate delivery from regional GW and demonstrated a need for measurement
112 techniques to identify variation in the texture of riverbeds. The work presented here focused on an
113 area just below site C (Fig. 1), which was shown to be a zone of regional GW up-welling, and
114 therefore a zone of legacy nitrate loading to the river (Binley et al., 2013).

115 2.2. Laboratory measurements

116 Seven 0.8 to 1.0 m core samples were extracted from the study site using a Cobra TT drill (Atlas
117 Copco, Stockholm, Sweden), see Fig. 1. The transition of the alluvial gravels (ALV) and underlying red
118 sands (RS) was abrupt which allowed for sub-sampling in the field. Samples were cut into
119 approximately 10 cm sections and double bagged before storage in a refrigerator; in total forty-five
120 samples were obtained. Samples were compressed during drilling but by assuming a linear
121 compression, the average thickness of the ALV was calculated as 0.35 m; the thicknesses were
122 relatively consistent and had a standard error (SE) of 0.04 m.

123 A total of nine ALV and eight RS samples were selected randomly for SIP, grain size distribution (GSD),
124 specific surface area, and CEC measurements. ALV samples were dry sieved with the following size
125 fractions: 45, 22.4, 11.2, 5.6, 4, 3.35, 2.8, 2.38, 1.7, 1.4, 1.18, and 1 mm. Sub-millimeter ALV samples
126 and RS samples were analyzed with a Beckman Coulter 13320 laser granulometer (Brea, California,

USA). Laser granulometer data and sieving data for ALV samples were combined assuming a homogeneous density of grains (2.65 g/cm^3).

Specific surface area was determined by nitrogen gas adsorption (Brunauer et al., 1938) using a Micrometrics Gemini VI 2385C instrument (Norcross, Georgia, USA). Samples were sieved to < 4 mm to fit the sample holder (diameter = 5 mm) and 2 g of each sample were loaded into each holder before analysis. To ensure samples were representative the quartering method was used (see Schumacher et al., 1990), also three replicates of an ALV sample and an RS sample were measured to ensure sampling errors were low. As with the specific surface area analysis, for CEC analysis samples were sieved to < 4 mm, quartered into 4 g samples, and CEC estimates were obtained using the sodium acetate method (see Chapman, 1965) and a flame photometer.

SIP measurements were made using an Ontash and Ermac PSIP device (River Edge, New Jersey, USA) and a Zimmerman ZEL SIP device (Zimmerman et al. 2008). For both devices, measurements were made at frequencies ranging from 10 mHz to 1 kHz, and several repeat samples were measured on both devices to ensure their consistency. Before SIP measurements, samples were rinsed several times using deionized water and saturated with 0.05 M sodium chloride solution for at least 12 hours. The sodium chloride concentration was selected to ensure that the electrical conductivity (48 mS/m) was consistent with observed pore fluid conductivity at the site (see Dudley-Southern and Binley, 2015). Samples were loaded into the holder and the current was injected between two copper coil electrodes, the potential was then measured with two silver-silver chloride point electrodes (Fig. 2). For the ALV samples measurements were made on samples sieved to < 4 mm and < 22.4 mm. The first grain-size threshold is used to match the limitations of the apparatus for specific surface area measurements; the second grain-size threshold provides electrical values more relevant to field conditions.

2.3. Synthetic modeling.

In all synthetic cases, the geoelectrical values used to represent the riverbed were chosen based on the SIP measurements at 2 Hz (i.e. the measurement frequency used in the field), and the conductivity used to represent the river was the value measured in the field (see section 2.4). Furthermore, in all cases, synthetic data are generated and inverted using cR2 or its 3D equivalent cR3t (Binley, 2018). These inversion algorithms minimize the L2 norm of the parameter space and use finite element meshes, which were generated using Gmsh (Geuzaine and Remacle, 2009), to model the voltages resulting from a dipolar current injection. These algorithms also permit the

158 blocking of regularization across specified regions, e.g. the river-riverbed interface, through reduced
159 local sensitivity.

160 2.3.1. Measurement sensitivity to river stage and riverbanks.

161 Firstly, the sensitivity of ERI and IP measurements to water column height was determined by
162 generating data for a two-layer model. The river was represented by a layer with a thickness, s, a
163 conductivity of 50 mS/m, and a phase angle of 0 mrad, and the riverbed was represented by a semi-
164 infinite unit with a 13.33 mS/m conductivity and an 8 mrad phase angle. Data were generated for
165 different dipole-dipole measurements with electrode spacing, *a,* and separation of the current and
166 voltage dipoles, *na,* assuming the electrodes are located on the upper surface of the riverbed for
167 three cases: $s = 0$ (i.e. no river present), $s = a$, and $s = 2a$. Additionally, to illustrate the effect of the
168 water column on the measurement, the measurement sensitivity, *S*, was computed according to
169 (see Binley, 2015):

170 $$S(x,z) = \frac{\partial log(\rho_a)}{\partial log(\rho(x,z))}, \quad (1)$$

171 where $\rho(x, z)$ is the resistivity at a given location (x, z), and ρ_a is the apparent resistivity. Furthermore,
172 by integrating $S(x, z)$ over a given depth z for all values of x, a vertical sensitivity profile can be
173 calculated.

174 Whilst it is intuitive that larger electrode separations will be more sensitive to deeper depths (e.g.
175 Day-Lewis et al., 2006), they will also have increased lateral sensitivity. Although assumptions behind
176 the 2D inversion of geoelectrical surveys in sub-aerial investigations are often valid, the presence of
177 a conductive water column means that measurements may be sensitive to riverbanks, especially in
178 narrow, upper course rivers. This effect was investigated by computing the response of dipole-dipole
179 measurements with electrode separation, a, for 3D models with different river widths (0, 0.5, 1, 1.5,
180 2, 3, 4.5, 7, and 10 m) using cR3t. The river channel was assumed orthogonal with a stage of 0.5 m,
181 the river was assigned a 50 mS/m conductivity, and a 0 mrad phase angle, the riverbed and riverbank
182 were both assigned a 13.33 mS/m conductivity and an 8 mrad phase angle.

183 2.3.2. Regularization across the river-riverbed interface.

184 To assess the impact of constraining river properties in the inversion, a three-layer case was used to
185 represent the field site. It comprised a 0.6 m thick layer with a 50 mS/m conductivity and a 0 mrad
186 phase angle, a 0.35 m thick layer with a 13.33 mS/m conductivity and an 8 mrad phase angle, and a
187 semi-infinite layer with a 20 mS/m conductivity and an 11 mrad phase angle. Data were generated
188 for a dipole-dipole array with 297 measurements; resistance values and phase angles were

corrupted with 1% and 0.1 mrad Gaussian noise, respectively. Data were then inverted using cR2 allowing for: (1) regularization across the river-riverbed interface, (2) separate regularization in the river and riverbed, and (3) constraint of river elements, to the known geoelectrical values, with separate regularization in the river and riverbed. Additionally, to assess the impact of data with poorer quality, the synthetic data was also corrupted with higher noise levels, 2.5%, and 1 mrad, respectively, and inverted with the same regularization scenarios as above.

As well as errors in geoelectrical data, measurements of river conductivity and stage may be incorrect. Although not necessarily relevant for this field site, given that stage can be accurately measured, larger-scale surveys may use acoustic sensors for bathymetric determination and may be prone to errors. Similarly, while it is reasonable to assume that for shallow cases the river conductivity is homogeneous, it is possible to obtain poor measurements from a faulty conductivity meter or have a field site where significant stratification exists, e.g. in lakes (e.g. Dahlin and Loke, 2018) or at the confluence of large rivers. However, it also important to note that similar issues could arise in shallow river environments when time-lapse ERI is used to monitor saline tracers (e.g. Ward et al., 2010) as it could be that the tracer is not well mixed.

To investigate the impact of inaccurate river properties on inverted ERI and IP results, data were generated from a two-layer model with a 0.6 m thick layer with a 50 mS/m conductivity and a 0 mrad phase angle, and a semi-infinite layer with a 13.33 mS/m conductivity and a phase angle of 8 mrad. As before, transfer resistances and phase angles were corrupted with 1% and 0.1 mrad Gaussian noise, respectively. Five scenarios were then tested and in each case, the river properties were constrained: (1) correct river depth and a correct river conductivity; (2) an incorrect river conductivity of 45 mS/m (i.e. 10% lower than the true value) with correct river depth; (3) an incorrect river conductivity of 55 mS/m (i.e. 10% higher than the true value) with the correct river depth; (4) an incorrect river depth of 0.54 m (i.e. 10% lower than the true value) with the correct river conductivity; (5) an incorrect river depth of 0.66 m (i.e. 10% higher than the true value) with the correct river conductivity. In all cases, no regularization across the river-riverbed interface was permitted.

2.4. Field-based geoelectrical data collection.

Field-based frequency-domain IP measurements were made using a Geolog2000 GeoTOM MK7E100 instrument (Geolog, Augsburg, Germany). Twenty-four 4 cm long stainless-steel bolts were punched through a 6 cm wide rubber belting with 25 cm spacing, this was done to aid with positioning along the center of the riverbed, parallel to flow direction. Stainless-steel electrodes were chosen as they

have been shown to provide good quality data (e.g. Dahlin et al., 2002); additionally, they are more robust than graphite and more practical than non-polarizing lead-lead chloride electrodes, especially in an aquatic environment with a gravel bed. Each electrode was wired using copper wire, run parallel along the rubber belting, and connected to the GeoTOM instrument. Although they were insulated; the cables were non-shielded. The array was placed onto the riverbed and electrodes were driven into the bed; rocks were placed between some electrodes to prevent the array from floating. A dipole-dipole sequence comprising 297 normal measurements, and 297 corresponding reciprocal measurements, was used. Current with a frequency of 2 Hz was injected with a range of 10 to 100 mA and the survey lasted 50 minutes. The river stage above each electrode was measured after the survey, and the electrical conductivity of the river water was measured both before and after the survey, at multiple locations to ensure it was consistent.

Reciprocal measurements were used to calculate a mean transfer resistance and phase angle for each quadrupole. Also, reciprocal errors were calculated from the difference between direct and reciprocal measurements. Transfer resistance measurements with > 10% error were removed, resulting in a total of 294 measurements with an average error of < 2.5%; for the phase angle measurements, measurements with > 25% error were removed, resulting in 63 measurements with an average absolute error of 0.6 mrad.

To model resistance errors for the inversion, measurements were grouped into 15 bins of equal size. The average error and resistance were determined for each bin and a linear model was fitted; the model exhibited an expected relationship of increasing error with increasing resistance magnitude. For phase errors it is common to find a parabolic relationship (e.g. Mwakanyemale et al., 2012), however, in this case, no correlation was observed, instead, a phase error of 0.6 mrad (i.e. the average absolute error) was assigned for weighting in the inversion.

Before the inversion, forward modeling errors (due to mesh discretization) were determined (e.g. LaBrecque et al., 1996) and added to error weights for both resistance and phase components. Smoothing across the river and riverbed was prevented and the river was constrained to a conductivity of 50 mS/m, as measured in the field, and the phase angle was constrained to 0 mrad. Due to the discrepancy in the number of measurements following filtering, the resistance data were first inverted to obtain a resistivity model using R2, this was subsequently used as a starting model for the inversion of resistance and phase data using cR2.

3. Results

3.1. Lab results

253 The grain size data are shown in Fig. 3; the RS samples were well sorted and had a mean grain size
254 of 0.255 (SE = 0.008) mm, whereas the ALV samples had significantly higher variability and an
255 average grain size of 4.792 (SE = 1.454) mm. For the ALV samples sieved to < 4 mm, the mean grain
256 size was 0.413 (SE = 0.043) mm.

257 The specific surface area, CEC, real conductivity, complex conductivity, and phase angles, at 2 Hz, for
258 RS and < 4 mm ALV samples are presented in Table 1. The specific surface area of RS and < 4 mm ALV
259 samples were not significantly different from one another, 3.02 (SE = 0.15) m^2/g and 2.84 (SE = 0.34)
260 m^2/g, respectively. Similarly, the CEC values for RS and < 4 mm ALV were not significantly different,
261 3.07 (SE = 0.24) meq/100 g and 2.87 (SE = 0.12) meq/100 g, respectively.

262 The spectral behavior for the RS, < 4 mm ALV, and < 22.4 mm ALV samples were distinctive and
263 displayed similar patterns for each sample type; the results of an ALV sample (C2.2) and an RS sample
264 (C2.5) are shown in Fig. 4 to highlight the typical spectra observed. All samples showed the expected
265 increasing real conductivity with increasing frequency. The real conductivity of the RS samples was
266 consistently higher than the < 22.4 mm ALV samples; however, in removing the > 4 mm particles;
267 the real conductivity behavior of the < 4 mm ALV samples became less distinguishable from the RS
268 samples. In terms of phase angle, the removal of coarser ALV fractions resulted in a slightly higher
269 phase angle. The contrasts between RS and ALV samples were greatest at higher frequencies (100-
270 1000 Hz) and indistinguishable at lower frequencies (0.05 to 0.1 Hz). Given the generally higher
271 conductivity and phase angle of RS samples, compared to ALV samples, the RS samples typically had
272 a higher polarization.

273 The imaginary conductivity, at 2 Hz is strongly correlated with specific surface area, expressed in
274 terms of m^2/g (see Fig. 5a). The specific surface area measurement of C2.2 was excluded as it was
275 deemed an outlier by Grubbs' (1950) outlier test (data was assumed normal, i.e. Shapiro-Wilk p-
276 value > 0.05), the resultant relationship had an R^2 of 0.74. Also, although not as strong (R^2 = 0.34),
277 imaginary conductivity was positively correlated with CEC (see Fig. 5b).

278 Most published relationships between imaginary conductivity and specific surface area use pore
279 normalized surface area, S_{por} (e.g. Weller et al., 2010). Specific surface area values without pore
280 normalization are presented in Fig. 5a as the porosity of each sample was not measured directly and
281 the surface area expressed in m^2/g is more commonly used in GW-SW interaction studies. However,
282 to compare with published results, the porosity of each sample was estimated assuming a grain
283 density of 2.65 g/cm^3, and from measurements of sample mass and core volume. Furthermore,
284 although not measured, the specific surface area of < 22.4 mm ALV samples can be estimated by

assuming > 4 mm grains are spherical. In doing so their specific surface area, expressed in m^2/g, becomes negligible. Subsequent normalizing for pore space results in an average S_{por} value of 6.58 1/µm for < 22.4 mm ALV and 18.08 1/µm for RS samples.

Expressed in these units, data can be compared with Weller et al. (2010) who presented an empirical link between S_{por} and imaginary conductivity following analysis of a large database of SIP measurements of sand and clay mixtures. Using pore fluids with a conductivity of 100 mS/m and an excitation frequency of 1 Hz, they found that $\sigma'' = 0.01\ S_{por}$ (where σ'' is expressed in mS/m and S_{por} is expressed in 1/µm). To account for the lower conductivity of the saturating fluid used here, the correction factor proposed by Weller et al. (2011) can be used such that $\sigma'' = 0.01 \sqrt{\sigma_w/\sigma_f}\ S_{por}$ (where σ_w is the conductivity of water used by Weller et al. (2010), i.e. 100 mS/m, and σ_f is the conductivity of the fluid used here, 48 mS/m). From this relationship the mean of the predicted S_{por} values for < 22.4 mm ALV and RS samples would be 20.21 and 50.51 1/µm, respectively. Although these are substantially higher than the observed S_{por}, these values fall within the data used by Weller et al. (2010) to fit their linear regression (see Fig. 2 of Weller et al., 2010).

3.2. Synthetic modeling

The results of the sensitivity of measurements to different river stages are shown in Fig. 6. It is evident that the water column suppresses the observed response; this is especially true of the phase angles. This effect may amplify the low signal-to-noise ratio typical of IP data and hence the collection of data with high error levels seems likely in aquatic environments.

It can also be noted that when $n = 1$, the apparent conductivity and phase angle for $s = a$ and $s = 2a$ are almost identical. This indicates that when $s \geq a$, river stage does not influence the response, i.e. the electrical flow boundary of the upper surface of the river is insignificant. It is also logical that if floating electrodes were used in this synthetic experiment, when $s \geq a$, the sensitivity of measurements to the riverbed would be negligible. Furthermore, although there is some sensitivity to the riverbed when using electrodes placed on the riverbed, it is evident that most sensitivity is within the water column. Moreover, it is evident from Fig 6c that there is a zone of reduced local sensitivity at the river-riverbed interface. Although this case uses a river conductivity of 50 mS/m, for cases where conductivity is larger it can be anticipated that sensitivity to a 13.33 mS/m riverbed would be reduced, in comparison sensitivity to the riverbed would increase for scenarios when river conductivity is lower.

315 In Fig. 7 the results of the case to investigate the sensitivity of measurements to riverbanks for
316 orthogonal channels are presented. It is evident that when $a = 0.5$ m, measurements are influenced
317 by the bank when the river width is less than ~2 m. For instance, assuming the channel is orthogonal,
318 data with electrode separations of $< 0.5\ m$ could be inverted using a 2D inversion algorithm. Similar
319 observations are also evident when $a = 1\ m$ and $a = 1.5\ m$, where the inversion could be treated as
320 2D when the river width is $< 4\ m$ and $< 6\ m$, respectively. Therefore, for the field data collected here,
321 and under the assumption of an orthogonal channel, inversion of the field data with a 2D inversion
322 algorithm was valid. However, as with the case presented in Fig. 6, it should be noted that these
323 results are for a river with a conductivity of 50 mS/m, for instance when the river conductivity is
324 lower the influence of banks may be more prevalent.

325 The effect of constraining river properties is presented in Fig. 8; the three-layer models used to
326 generate data are shown in Fig. 8a and 8b. It is evident that allowing regularization across the river-
327 riverbed interface gives a poorly resolved conductivity model (Fig. 8c) where the upper riverbed
328 layer appears more conductive than the lower layer; a similar effect is seen for the phase angle
329 model (Fig. 8d). Adding the river-riverbed boundary and enforcing a separation in the regularization
330 results in the conductivity of the river (Fig. 8e) being recovered more accurately, but the riverbed
331 appears as a broadly homogeneous layer for both conductivity (Fig. 8e) and phase angle (Fig. 8f)
332 images. This highlights the observations from Fig. 6, that measurements are relatively insensitive to
333 riverbed properties and that data can be fitted easily by modifying parameters of the river layer.
334 When river values are constrained in the inversion, the inverse model is significantly improved and
335 reveals a contrast in the two riverbed layers with a reasonable demarcation of the two units,
336 particularly for the conductivity image (Fig. 8g). However, if data have higher noise levels, the
337 contrast in the two units is weakened and demarcation of the lower unit is less obvious in the
338 conductivity (Fig. 8i) and phase angle (Fig. 8j) images, this highlights the importance of good quality
339 data.

340 The effects of incorrect constraining of river properties are presented in Fig. 9. Results of the
341 constrained inversion using the correct river values are shown in Fig. 9a and 9b, where the two-layer
342 structure is well resolved. Constraining the river conductivity to a value that is too low forces the
343 inversion to compensate by resolving the riverbed as more conductive (Fig. 9c) and less polarizable
344 (Fig. 9d) than it ought to be. In this case, the inverted phase angle is lower than in Fig. 9b because
345 the synthetic data are less sensitive to the riverbed (i.e. they contain less information about the
346 riverbed) than is accounted for by the inversion, such that the riverbed phase angle values are

underestimated. Conversely, by setting the conductivity of the river too high the inversion creates a non-existent low conductivity layer (Fig. 9e), and in the phase angle image the phase angle values are elevated (Fig. 9f). Similar effects are also seen with erroneous depth fixing, underestimation of river depth results in a resistive artifact near the riverbed followed by a more conductive underlying region (Fig. 9g). In comparison, the overestimation of the river stage results in an overly resistive upper riverbed with high phase angles, and overly conductive lower riverbed with low phase angle values, Fig. 9i and 9j respectively.

3.3. Field results

The inverted models for the field data, expressed in real conductivity and phase angle, are shown in Fig. 10. Based on laboratory values obtained at 2 Hz, it was anticipated that the riverbed would be characterized by two-layers, with the ALV exhibiting a conductivity of 13.33 mS/m, a phase angle of 8 mrad, and a thickness of ~0.35 m overlying the RS layer with a conductivity of 20 mS/m and a phase angle of 11 mrad. The most obvious boundary in the inverted real conductivity is at approximately 1 m below the river-riverbed interface. This boundary separates an upper region with average real conductivity values of 20-40 mS/m and a lower region with average real conductivity values of 4-10 mS/m. Additionally, although more subtle, there is a distinction between a lower conductivity zone immediately beneath the river and the underlying 20-40 mS/m region. In comparison, the phase angle image is dominated shows a polarizable region and an underlying region with lower phase angles. In particular, the upper region is characterized by high phase values at a horizontal location of 1.5 to 3 m.

4. Discussion

4.1. Characterization of units within the riverbed

It was demonstrated, via synthetic modeling, that constraining river properties with accurate values resulted in a more accurate determination of the geoelectrical properties and better demarcation of the boundary within the riverbed. However, constraining the river with erroneous values in the inversion resulted in misleading artifacts. Although, simply preventing regularization across the river-riverbed interface (i.e. without constraining river properties), provided river conductivity and phase angle values comparable to the values of the synthetic model used to generate the data it was not possible to differentiate between the subtle contrasts in the riverbed (see Fig. 8e and 8f). Potentially, the decision to limit regularization across the river-riverbed interface but allow the inversion to modify the geoelectrical properties of the river could be useful in environments where there are greater contrasts in geoelectrical properties (e.g. fluvial sediments overlying electrically

resistive bedrock). Also, although in this work the field data were collected for an electrical current injected at 2 Hz, potentially the collection of high-quality data at higher frequencies may have also aided in the demarcation of the units here, see Fig. 4b.

A major issue of the inversion is when the water column properties (i.e. stage and conductivity) are erroneously constrained as they will result in horizontal artifacts. This makes it difficult to distinguish between genuine geological units and inversion artifacts. For instance, unless intrusive data are also collected such artifacts will likely be interpreted as stratigraphic units. These artifacts also become clear in time-lapse cases, this problem was encountered in McLachlan et al. (2020) where extreme resistivity changes in sequential data sets could not realistically be explained by hydrological or biogeochemical processes. Although not investigated here, similar artifacts are also likely to be generated in cases where surface waters are poorly mixed, e.g. cases where stratification is present or in time-lapse ERI/IP experiments where saline tracers have not fully mixed with the river water.

Moreover, whilst it is possible to dampen the presence of these artifacts by increasing the error weighting in the inversion, the fictitious stratigraphy effect would merely be subdued and it could still obscure the interpretation of genuine lithological structures. In the context of the field data here, the real conductivity image of the riverbed can be interpreted in terms of three lithological units. An upper layer with a thickness of 0.2-0.4 m and an average conductivity of 5-20 mS/m, a middle layer with a thickness of 0.6-0.8 m and an average conductivity of 30-40 mS/m, and a lower layer with a conductivity of 5-10 mS/m. This could be interpreted in terms of the expected geology of the site, i.e. ALV, RS, and the underlying Penrith Sandstone bedrock; however similar features could also be created if the actual river conductivity was lower than the value that was measured and used to constrain the inversion (e.g. Fig. 9e). Furthermore, although the reciprocal errors for measured resistances were relatively low (< 2.5 %), based on the results from Fig. 8i a clear boundary between the ALV and RS units would not be expected.

4.2. ERI an IP data quality

In the synthetic studies to assess inversion decisions, it was assumed that data was relatively high quality (i.e. 1% for resistance and 0.1 mrad for phase angle). However, when data with higher error (i.e. 2.5% and 1 mrad) were considered, the ability to distinguish between the ALV and RS, and obtain accurate geoelectrical properties were substantially reduced. In the field data here, ~80% of phase angle measurements had errors exceeding 25%, and only ~20% of data were inverted. One shortcoming of this work is that methods to collect higher quality phase data were not investigated. For instance, although objective tests of electrode material have been conducted in sub-aerial IP

investigations (e.g. Dahlin et al., 2002; Zarif et al., 2018), similar work has not been conducted for aquatic systems. Nonetheless, it is important to note that in their characterization of a riverbed using IP, Benoit et al. (2019) achieved high-quality data using a floating array of stainless-steel electrodes. Another reason for poor quality IP data could be the presence of non-shielded cables that were run in proximity to one another along the array and through the river; potentially this led to significant coupling and poor-quality phase angle measurements. Future applications should attempt to explore the effects of electrode materials, measurement geometry (Martin et al., 2020), and the use of shielded cables (e.g. Flores Orocozo et al., 2013) on geoelectrical data quality in aquatic environments.

Another important aspect of this work was that reciprocity checks enabled the characterization of errors. Although the importance of appropriate data weighting in inversions of aquatic geoelectrical data was not explored in this work, it is also perhaps an important area for future synthetic studies given the sensitivity of measurements to the water column. This is especially true for studies employing towed arrays where the collection of reciprocal measurements is not possible. It is anticipated that, as with standard sub-aerial applications, overestimation of errors would lead to overly smoothed models of the subsurface, whereas the underestimation of errors could exacerbate artifacts related to the issues surrounding the water column.

4.3. Comparing laboratory and field observations

One of the aims of this work was to apply laboratory-derived petrophysical relationships to field data. The laboratory measurements indicated the potential of IP to characterize important properties of riverbed sediments relevant to GW-SW interactions. Despite the similar specific surface area values of RS and < 4 mm ALV samples, they were strongly correlated with the imaginary conductivity values (Fig. 5a). Furthermore, in re-scaling the surface area measurements for ALV samples with grains > 4 mm the link between S_{por} and polarization was found to follow published relationships for sands and sandstones (Weller et al., 2010).

The elevated phase angle values in the inverted field data (Fig. 10b) are unlikely to relate to natural (e.g. sedimentological) features. For instance, although the elevated phase angles could be attributed to finer particles in the ALV than were sampled during drilling, this is unlikely as samples were collected in a plastic sheath, this meant that the loss of fine materials was minimal. Moreover, the phase angle values in the field ought to be smaller because > 22.4 mm grains were not measured in the laboratory. These elevated values are most likely related to issues with data quality.

Nonetheless, when the field data is expressed in terms of imaginary conductivity (Fig. 11a) it is evident that values are dominated by the real conductivity. For instance, the high phase angle values observed in Fig. 10b are coincident with areas of low conductivity When applying the laboratory-derived petrophysical model (Fig. 11b) the riverbed appears to comprise a layer with a moderate specific surface area, overlying a layer of, comparatively, higher specific surface area, and an underlying unit of low specific surface area. However, it is important to note that this relationship is based on measurements of RS and < 4 mm ALV, and not < 22.4 mm ALV as measurements of the specific surface area of coarser fractions were not possible. Also, the maximum specific surface area measured in the laboratory was 3.76 m^2/g.

4.4. Recommendations for future work

Several important observations are made in this work that can help to inform future studies. These are summarized as follows:

- Practitioners should be aware of the limitations in the sensitivity of ERI and IP measurements, especially in deep waters or settings with high conductivity (e.g. saline) environments. It is important to consider this before inversion as constraining inversions with incorrect water column data could produce information about underlying lithology even if there is insignificant sensitivity to the bed. Post-inversion depth of investigation analysis (e.g. Oldenburg and Li, 1999) could be used to aid in the validation of results from deep water or high conductivity environments.
- Inaccurate knowledge of water column properties can result in the fabrication of non-existent lithological units. Although such artifacts may be avoided in some cases (e.g. beds with large contrasts in geoelectrical properties) simply preventing regularization across the riverbed in inversions may yield useful results. However, such an approach should be applied with caution.
- It was observed in the laboratory that the phase angle contrasts were greater for higher frequencies, however here field measurements were made with frequencies of 2 Hz. In most field investigations, measurements are typically made with frequencies in the order of 1-2 Hz predominantly due to instrumentation limitations and the higher error levels commonly encountered for high-frequency measurements (see Martin et al., 2020). It is, however, anticipated that improvements in instrumentation and acquisition strategies will provide future opportunities for enhanced characterization.

- The sensitivity of measurements to riverbanks demonstrated that, under the assumption of an orthogonal channel, inverting data with a 2D inversion algorithm was sufficient. However, channels may be characterized by significant off-axis variation in channel morphology. This is likely to have similar effects as erroneous constraining of the water column and may also lead to obscuration of the true geoelectrical structure. In areas with significant variability in bathymetry, inversions should perhaps be conducted using 3D algorithms. However, practically speaking this significantly reduces the efficiency of geoelectrical measurements over traditional intrusive sampling given that detailed bathymetric surveys may be time-consuming.
- Ideally, in terms of usefulness to GW-SW interaction studies, geoelectrical methods would be used to characterize larger areas to estimate bed properties at scales relevant to the catchment. However, given the complications of characterization for a relatively simple case presented here, e.g. a river with a homogenous conductivity and a stage that can be measured directly, applications at larger scales using towed or floating arrays should be particularly aware of the impact that inaccurate water column properties have on the inversion.

Acknowledgments

This work was supported by the NERC Envision Doctoral Training Program (GA/15S/004 S301). We acknowledge the field assistance of Michael Tso, Youliang Zhang, John McLachlan, and Jon Algeo, and the laboratory assistance of John Crosse, Simon Kemp, and Ian Mounteney. We also acknowledge the helpful comments of Fred Day-Lewis and two anonymous reviewers who provided detailed feedback on a previous iteration of the manuscript.

References

Allen, D. J., Bloomfield, J. P., Robinson, V. K., 1997. The physical properties of major aquifers in England and Wales, British Geological Survey Technical Report. WD/97/34:312, Natural Environment Research Council and Environment Agency.

Bencala, K.E., Kennedy, V.C., Zellweger, G.W., Jackman, A.P., Avanzino, R.J., 1984. Interactions of solutes and streambed sediment: 1. An experimental analysis of cation and anion transport in a mountain stream. Water Resources Research. 20, 1797–1803.

Benoit, S., Ghysels, G., Gommers, K., Hermans, T., Nguyen, F., Huysmans, M., 2019. Characterization of spatially variable riverbed hydraulic conductivity using electrical resistivity tomography and induced polarization. Hydrogeological Journal. 27, 395–407.

Binley, A. M., 2018. cR2 user guide [online] Available at: http://www.es.lancs.ac.uk/people/amb/Freeware/cR2/cR2_readme.pdf [08-April-2020].

Binley, A. (2015). Tools and Techniques: Electrical Methods. Treatise on Geophysics: Second Edition (Vol. 11). Elsevier B.V. https://doi.org/10.1016/B978-0-444-53802-4.00192-5

Binley, A., Keery, J., Slater, L., Barrash, W., Cardiff, M. (2016). The hydrogeologic information in cross-borehole complex conductivity data from an unconsolidated conglomeratic sedimentary aquifer. Geophysics, 81(6), E409–E421. https://doi.org/10.1190/GEO2015-0608.1

Binley, A., Ullah, S., Heathwaite, A.L., Heppell, C., Byrne, P., Lansdown, K., Trimmer, M., Zhang, H., 2013. Revealing the spatial variability of water fluxes at the groundwater-surface water interface: Spatial Variability of Groundwater-Surface Water Fluxes. Water Resources Research. 49, 3978–3992.

Brunauer, S., Emmett, P. H., Teller, E., 1938. Adsorption of gases in multimolecular layers. Journal of the American Chemical Society, 60:309-19.

Chapman, H.D., 1965. Cation Exchange Capacity. In: Black, C.A., Ed., Methods of Soil Analysis, American Society of Agronomy, Madison, 891-901.

Wang, C., Briggs, M. A., Day-Lewis, F. D., Slater, L. D., in review. In-Situ Characterization of Streambed Sediments from Complex Conductivity Measurements. Geophysical Research Letters

Crook, N., Binley, A., Knight, R., Robinson, D.A., Zarnetske, J., Haggerty, R., 2008. Electrical resistivity imaging of the architecture of substream sediments. Water Resources Research. 44.

Dahlin, T., Leroux, V., Nissen, J., 2002. Measuring techniques in induced polarisation imaging. Journal of Applied Geophysics. 50. 279-298. 10.1016/S0926-9851(02)00148-9.

Day-Lewis, F.D., White, E.A., Johnson, C.D., Lane Jr., J.W., Belaval, M., 2006. Continuous resistivity profiling to delineate submarine groundwater discharge - examples and limitations. The Leading Edge 25. (6), 724–729.

Dudley-Southern, M., Binley, A., 2015. Temporal responses of groundwater-surface water exchange to successive storm events. Water Resources Research 51, 1112–1126. https://doi.org/10.1002/2014WR016623

Flores Orozco, A., Gallistl, J., Bücker, M., Williams, K.H., 2018b. Decay curve analysis for data error quantification in time-domain induced polarization imaging. Geophysics 83 (2), E75–E86

Zimmermann, E., Kemna, A., Berwix, J., Glaas, W., Münch, H. M., Huisman, J. A., 2008. A high-accuracy impedance spectrometer for measuring sediments with low polarizability 19, 10

Gagliano, M.P., Nyquist, J.E., Toran, L., Rosenberry, D.O., 2009. Assessment of Electrical Resistivity Method to Map Groundwater Seepage Zones in Heterogeneous Sediments, in: Symposium on the Application of Geophysics to Engineering and Environmental Problems 2009. Presented at the Symposium on the Application of Geophysics to Engineering and Environmental Problems 2009, Environment and Engineering Geophysical Society, 815–823. https://doi.org/10.4133/1.3176773

Geuzaine, C., Remacle, J. F., 2009. Gmsh: a three-dimensional finite element mesh generator with built-in pre- and post-processing facilities. International Journal for Numerical Methods in Engineering 79(11), 1309-1331.

Grubbs, Frank E. (1950). "Sample criteria for testing outlying observations". Annals of Mathematical Statistics. 21 (1): 27–58. doi:10.1214/aoms/1177729885.

Harvey, Judson W., Gooseff, M., 2015. River corridor science: Hydrologic exchange and ecological consequences from bedforms to basins. Water Resources Research, 51(9), 6893–6922. https://doi.org/10.1002/2015WR017617

Heppell, C., Louise Heathwaite, A., Binley, A., Byrne, P., Ullah, S., Lansdown, K., Keenan, P., Trimmer, M., Zhang, H., 2014. Interpreting spatial patterns in redox and coupled water–nitrogen fluxes in the streambed of a gaining river reach. Biogeochemistry 117, 491–509. https://doi.org/10.1007/s10533-013-9895-4

Hördt, A., Blaschek, R., Kemna, A., Zisser, N., 2007. Hydraulic conductivity estimation from induced polarisation data at the field scale — the Krauthausen case history. Journal of Applied Geophysics 62, 33–46. https://doi.org/10.1016/j.jappgeo.2006.08.001

Käser, D.H., Binley, A., Heathwaite, A.L., Krause, S., 2009. Spatio-temporal variations of hyporheic flow in a riffle-step-pool sequence. Hydrological Processes 23 (15), 2138–2149. https://doi.org/10.1002/hyp.

Kelly, B.F.J., Allen, D., Ye, K., Dahlin, T., 2009. Continuous electrical imaging for mapping aquifer recharge along reaches of the Namoi River in Australia. Near Surface Geophysics 7, 259–270. https://doi.org/10.3997/1873-0604.2009024

561 Krause, S., Heathwaite, L., Binley, A., Keenan, P., 2009. Nitrate concentration changes at the
562 groundwater-surface water interface of a small Cumbrian river. Hydrological Processes 23, 2195–
563 2211. https://doi.org/10.1002/hyp.7213

564 LaBrecque, D. J., M. Miletto, W. Daily, A. Ramirez, and E. Owen, 1996, The effects of noise on Occam's
565 inversion of resistivity tomography data: Geophysics, 61, 538–548, doi: 10.1190/1.1443980

566 Lansdown, K., Heppell, C.M., Trimmer, M., Binley, A., Heathwaite, A.L., Byrne, P., Zhang, H., 2015.
567 The interplay between transport and reaction rates as controls on nitrate attenuation in permeable,
568 streambed sediments. Journal of Geophysical Research Biogeosciences. 120, 1093–1109.

569 Lansdown, K., Trimmer, M., Heppell, C.M., Sgouridis, F., Ullah, S., Heathwaite, A.L., Binley, A., Zhang,
570 H., 2012. Characterization of the key pathways of dissimilatory nitrate reduction and their response
571 to complex organic substrates in hyporheic sediments. Limnology and Oceanography. 57, 387–400.

572 Leroy, P., 2009. A mechanistic model for the spectral induced polarization of clay material. Journal
573 of Geophysical Research 114, B10202.

574 Martin, T., Thomas Günther, Adrian Flores Orozco, Torleif Dahlin, Evaluation of spectral induced
575 polarization field measurements in time and frequency domain, Journal of Applied Geophysics,
576 Volume 180, 2020,

577 McLachlan, P., Chambers, J., Uhlemann, S. and Binley, A., 2017. Geophysical characterisation of the
578 groundwater-surface water interface, Advances in Water Resources, 109, 302–319.

579 McLachlan, P., Chambers, J., Uhlemann, S., Sorensen, J. Binley, A., (2020). Electrical resistivity
580 monitoring of river-groundwater interactions in a Chalk River and neighboring riparian zone. Near
581 Surface Geophysics.

582 Mitchell, N., Nyquist, J.E., Toran, L., Rosenberry, D.O., Mikochik, J.S., 2008. Electrical Resistivity as a
583 Tool for Identifying Geologic Heterogeneities Which Control Seepage at Mirror Lake, NH, in:
584 Symposium on the Application of Geophysics to Engineering and Environmental Problems 2008.
585 Presented at the Symposium on the Application of Geophysics to Engineering and Environmental
586 Problems 2008, Environment and Engineering Geophysical Society, pp. 749–759.

587 Mwakanyamale, K., Slater, L., Binley, A., Ntarlagiannis, D., 2012. Lithologic imaging using complex
588 conductivity: Lessons learned from the Hanford 300 Area. Geophysics 77, E397–E409.

589 Orlando, L., 2013. Some considerations on electrical resistivity imaging for characterization of
590 waterbed sediments. Journal of Applied Geophysics 95, 77–89.

591 Revil, A., 2012. Spectral induced polarization of shaly sands: influence of the electrical double layer.
592 Water Resources Research. 48.

593 Revil, A., Karaoulis, M., Johnson, T., Kemna, A., 2012. Review: Some low-frequency electrical
594 methods for subsurface characterization and monitoring in hydrogeology. Hydrogeology Journal. 20,
595 617–658.

596 Schumacher, B.A., Shines, K.C., Burton, J.V., Papp, M.L., 1990. A Comparison of Soil Sample
597 Homogenization Techniques 49.

598 Slater, L., 2007. Near Surface Electrical Characterization of Hydraulic Conductivity: From
599 Petrophysical Properties to Aquifer Geometries—A Review. Surveys in Geophysics. 28, 169–197.

600 Slater, L.D., Ntarlagiannis, D., Day-Lewis, F.D., Mwakanyamale, K., Versteeg, R.J., Ward, A., Strickland,
601 C., Johnson, C.D., Lane, J.W., 2010. Use of electrical imaging and distributed temperature sensing
602 methods to characterize surface water–groundwater exchange regulating uranium transport at the
603 Hanford 300 Area, Washington. Water Resources Research. 46, 2010WR009110.

604 Snyder, D.D., Wightman, W.E., 2002. Application of continuous resistivity profiling to aquifer
605 characterization. In: Proceedings of the 15th Symposium on the Application of Geophysics to
606 Engineering and Environmental Problems. Las Vegas, Nevada, US

607 Triska, F.J., Duff, J.H., Avanzino, R.J., 1993. The role of water exchange between a stream channel and
608 its hyporheic zone in nitrogen cycling at the terrestrial-aquatic interface 18.

609 Ward, A.S., Gooseff, M.N., Singha, K., 2010. Characterizing hyporheic transport processes —
610 Interpretation of electrical geophysical data in coupled stream–hyporheic zone systems during
611 solute tracer studies. Advances in Water Resources. 33, 1320–1330.

612 Weller, A., Slater, L., Nordsiek, S., and Ntarlagiannis, D., 2010. On the estimation of specific surface
613 per unit pore volume from induced polarization: A robust empirical relation fits multiple data sets:
614 Geophysics, 75, WA105-WA112.

615 Weller, A., Slater, L.D., 2015. Induced polarization dependence on pore space geometry: Empirical
616 observations and mechanistic predictions. Journal of Applied Geophysics. 123, 310–315.

617 Wynn J. C., 1988. Titanium geophysics – The application of induced polarization to sea-floor mineral
618 exploration. Geophysics. 53, 386–401

Limitations and considerations for electrical resistivity and induced polarization imaging of riverbed sediments: Observations from laboratory, field, and synthetic experiments.

Table and Figure Captions

Table 1 – Laboratory data of < 4 mm ALV and RS samples, SIP measurements obtained from currents with a frequency of 2 Hz.

#	Type	Specific Surface Area (m^2/g)	CEC (meq/g)	σ' (mS/m)	σ'' (mS/m)	ϕ (mrad)
C1.2	ALV (< 4 mm)	2.30	3.83	12.46	0.14	10.87
C1.3	ALV (< 4 mm)	2.92	2.83	21.88	0.24	10.92
C1.6	RS	3.09	2.78	20.48	0.24	11.47
C2.1	ALV (< 4 mm)	2.24	1.84	13.89	0.13	9.36
C2.2	ALV (< 4 mm)	4.95	4.10	18.86	0.18	9.33
C2.4	RS	2.7	2.94	20.22	0.24	12.35
C2.5	RS	3.45	3.28	19.59	0.23	11.55
C2.6	RS	2.65	2.40	19.08	0.23	11.95
C2.8	RS	2.62	2.46	20.01	0.16	8.02
C4.1t	ALV (< 4 mm)	2.83	3.39	19.47	0.16	6.97
C4.2t	ALV (< 4 mm)	3.64	4.37	20.59	0.27	13.11
C4.2b	RS	3.76	3.21	-	-	-
C5.7	RS	2.73	2.67	18.79	0.15	7.90
C6.1	ALV (< 4 mm)	1.64	1.55	19.47	0.1	5.27
C6.3	ALV (< 4 mm)	3.08	3.26	20.96	0.27	12.86
C6.7	RS	3.13	3.21	20	0.27	13.64

C7.2	ALV (< 4 mm)	1.88	2.01	17.69	0.13	7.45

Layout instructions

Figure	Layout preference
1	Single column
2	Single column
3	Single column
4	Single column
5	Single column
6	Double column
7	Double column
8	Double column
9	Double column
10	Double column
11	Double column

Figure 1: Location of study site within a 200 m meander of the River Leith. The inset shows the position of the field site in the north of England, the flow direction is from site A to site I. The circular symbols indicate the position of the riverbed and riparian piezometers used in the study of Binley et al. (2013), see this work for additional analysis of site characteristics.

Figure 2: Cross-sectional schematic of the sample holder used for SIP measurements.

Figure 3: Grain size distribution of (a) RS samples and (b) ALV samples.

Figure 4: Representative SIP spectra for RS (C2.5), < 4 mm ALV (C2.2) and < 22.4 mm ALV (C2.2) for (a) real conductivity and (b) phase angle.

Figure 5: (a) Linear relationship between specific surface area and imaginary conductivity, and (b) linear relationship between CEC and imaginary conductivity.

Figure 6: Response of dipole-dipole measurements to different river stages: (a) apparent conductivity, (b) phase angle, and (c) measurement sensitivity.

Figure 7: Response of dipole-dipole measurements to different river widths: (a) schematic showing the central region of 3D mesh and electrode array, (b) apparent conductivity, and (c) phase angle.

Figure 8: Models for regularized, blocked, and constrained river element inversions. Synthetic models for real conductivity and phase are shown in (a) and (b). Inverse models for the lower noise case with regularization across the river-riverbed interface are shown in (c) and (d). Inverse models for the lower noise case with no regularization across the river-

riverbed interface are shown in (e) and (f). Inverse models for the lower noise case with no regularization across the river-riverbed interface and constrained river element properties are shown in (g) and (h). Inverse models for the higher noise case with no regularization across the river-riverbed interface and constrained river element properties are shown in (i) and (j). The dashed lines indicate the position of the 2nd and 3rd layer boundary and electrode positions are marked by white circles.

Figure 9: Inversion results with the erroneous constraining of river properties. Inverted models for when the river conductivity and river depth are correctly constrained are shown in (a) and (b). Inverted models when the river is erroneously constrained to 10% underestimation in real conductivity are shown in (c) and (d). Inverted models when the in the river is erroneously constrained to a 10% overestimation in real conductivity are shown in (e) and (f). Inverted models with a 10% underestimation in river depth are shown in (g) and (h). Inverted models with a 10% overestimation in river depth are shown in (i) and (j).

Figure 10: Inverted field data: (a) real conductivity and (b) phase angle.

Figure 11: Petrophysical transformation of data in terms of specific surface area, using laboratory relationship present in Figure 5a.

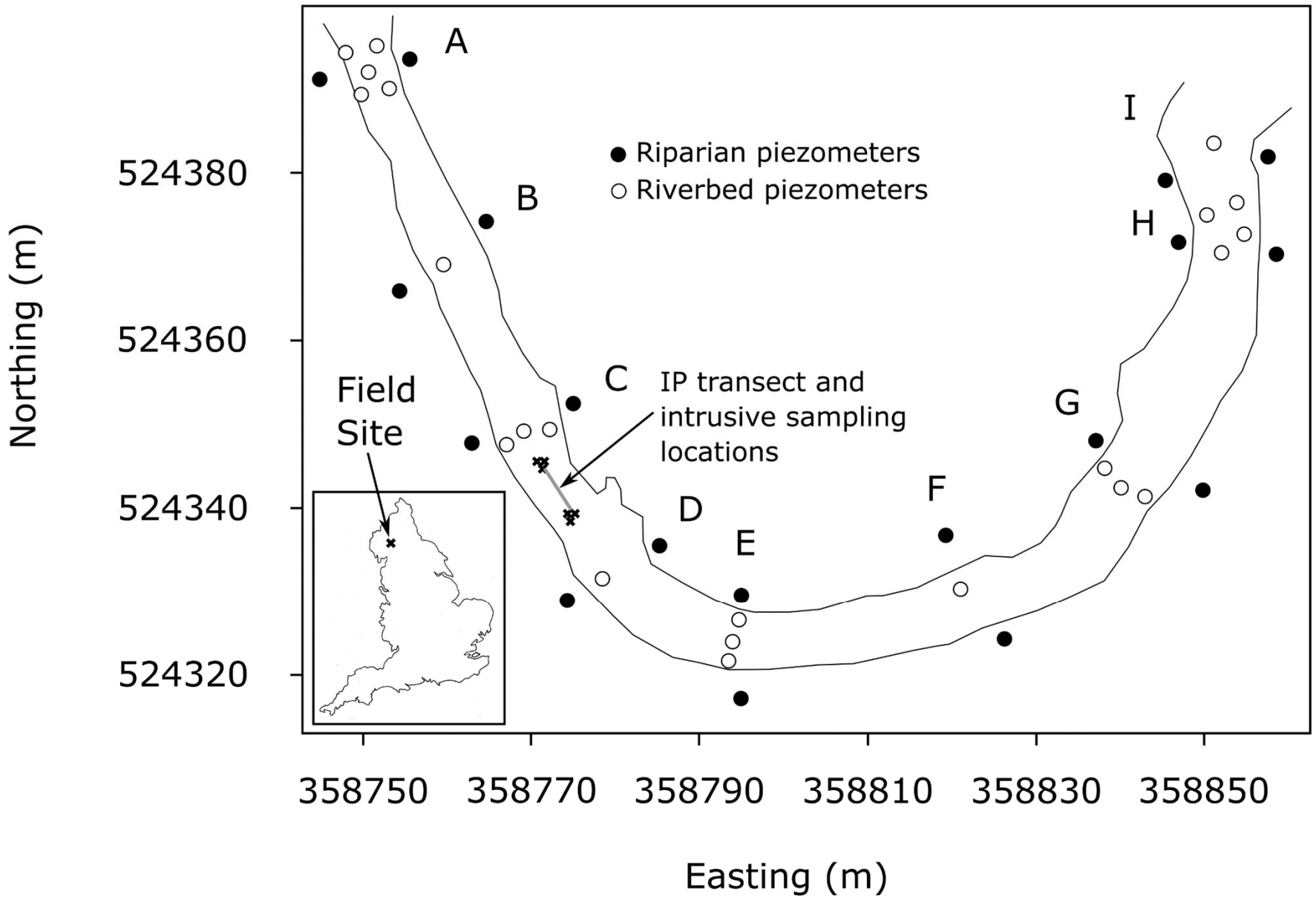
A
B
C
D
E
F
G
H
I
Riparian piezometers
Riverbed piezometers
IP transect and
intrusive sampling
locations
Field
Site
524380
524360
524340
524320
Northing (m)
358750
358770
358790
358810
358830
358850
Easting (m)

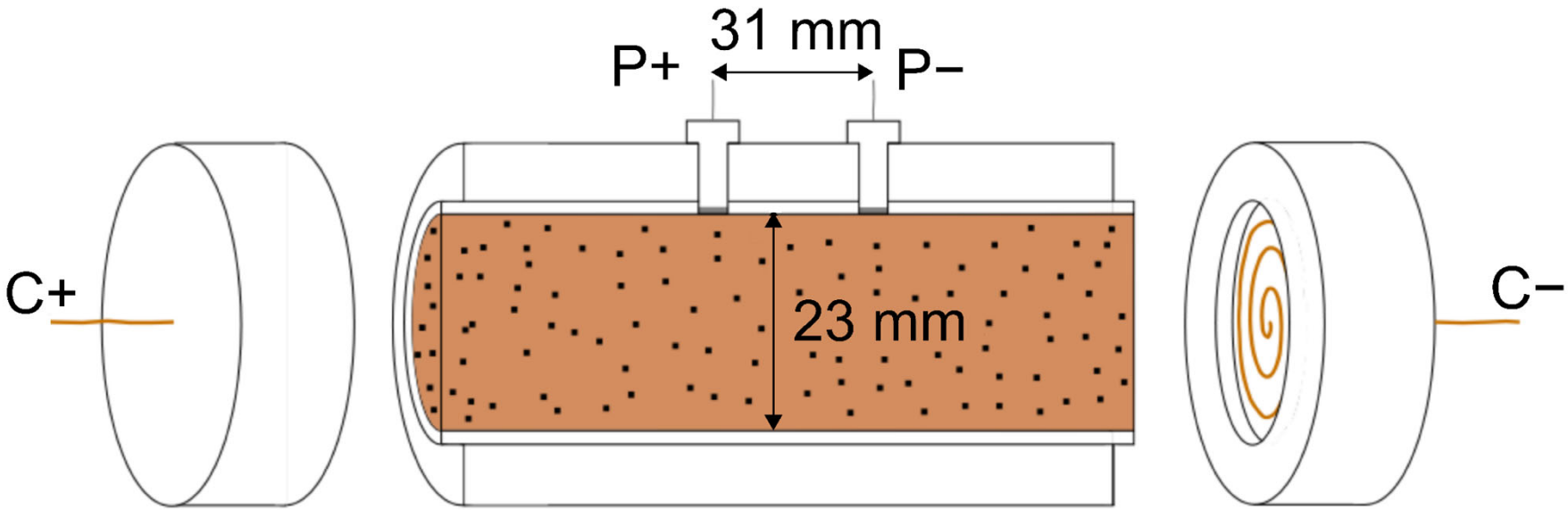
31 mm
P+
P−
C+
C−
23 mm

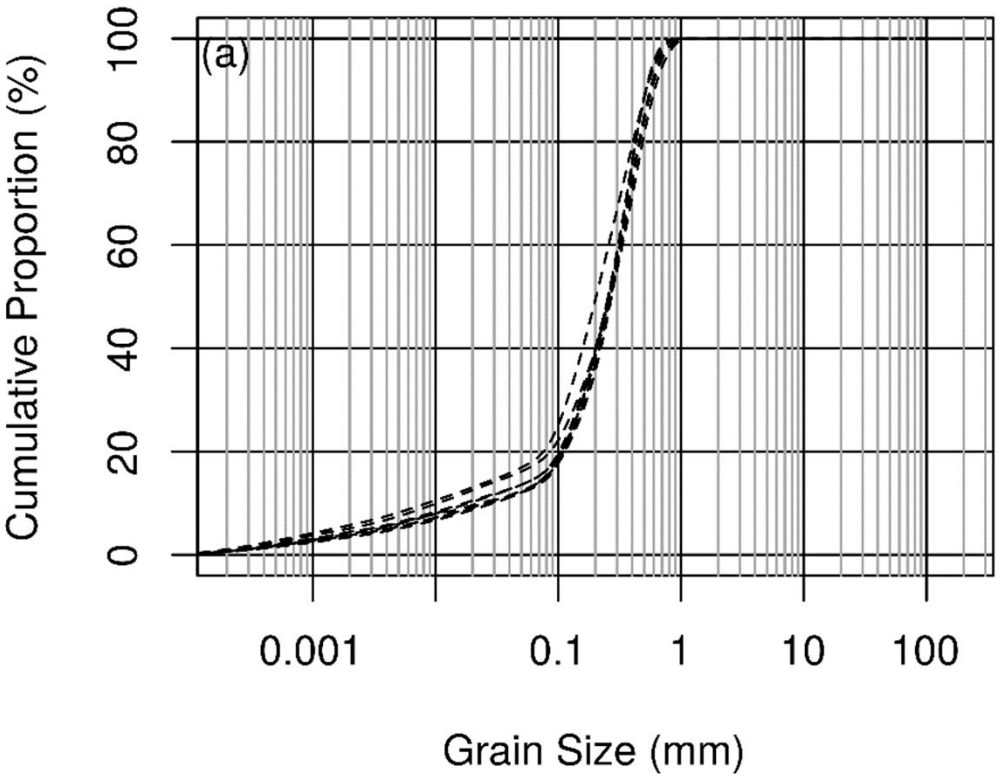
(a)
Cumulative Proportion (%)
0
20
40
60
80
100
0.001
0.1
1
10
100
Grain Size (mm)

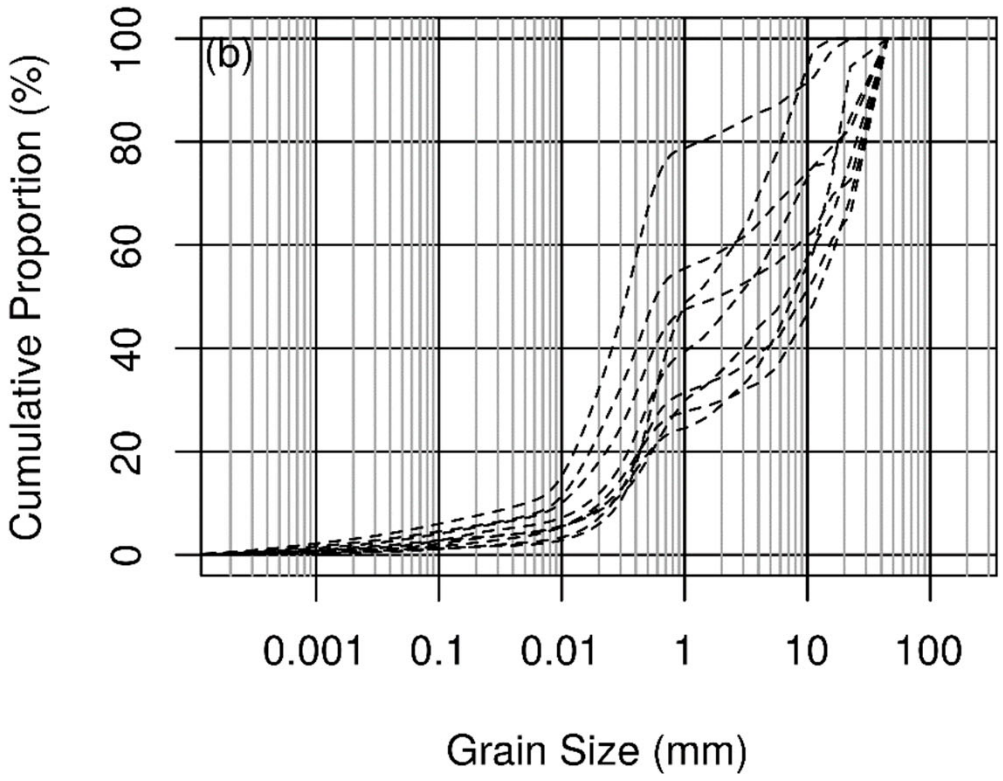
(b)
Cumulative Proportion (%)
0
20
40
60
80
100
0.001
0.1
0.01
1
10
100
Grain Size (mm)

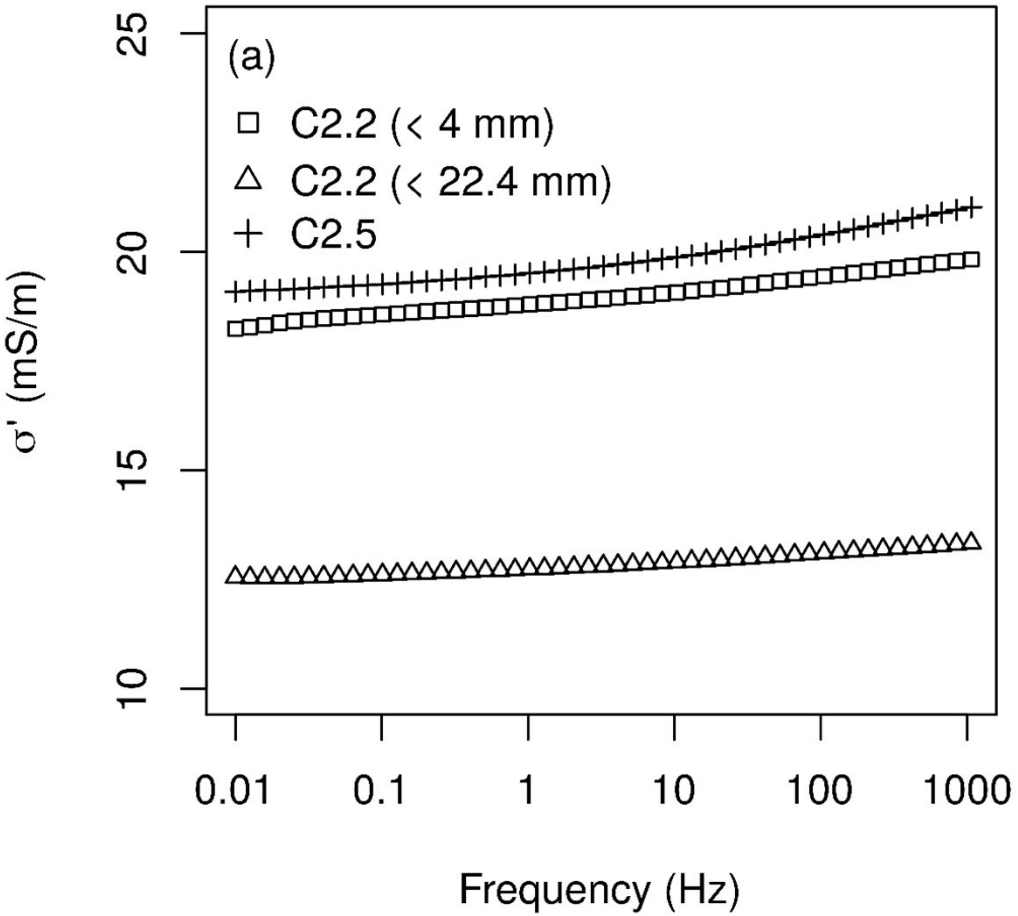
(a)
C2.2 (< 4 mm)
C2.2 (< 22.4 mm)
C2.5
σ' (mS/m)
10
15
20
25
0.01
0.1
1
10
100
1000
Frequency (Hz)

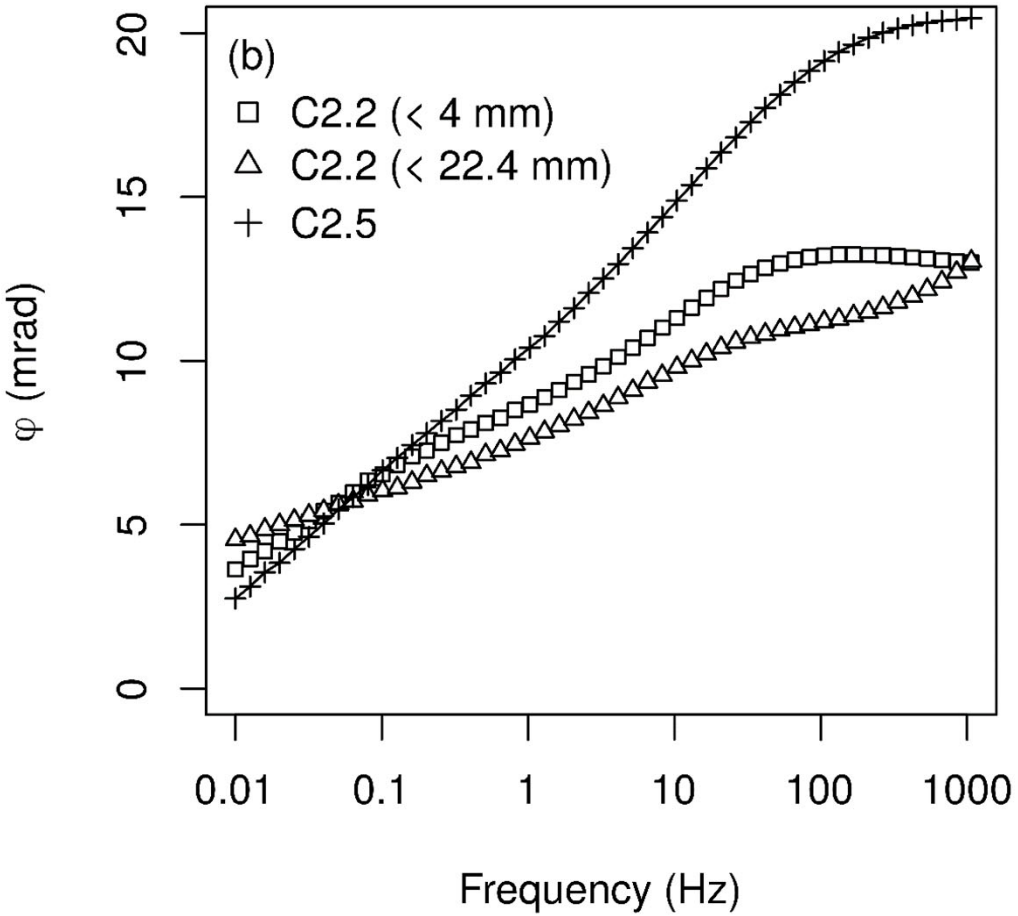
(b)
C2.2 (< 4 mm)
C2.2 (< 22.4 mm)
C2.5
φ (mrad)
0
5
10
15
20
0.01
0.1
1
10
100
1000
Frequency (Hz)

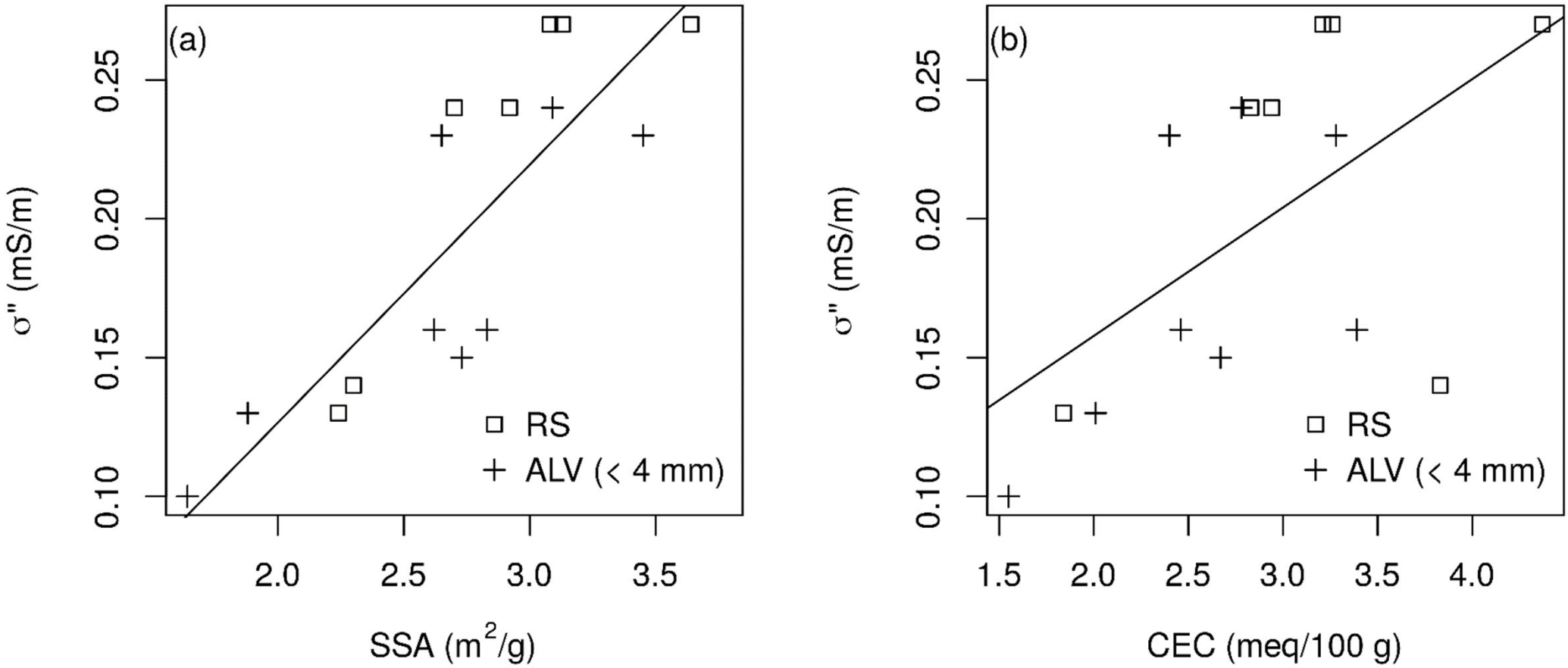
(a)
σ" (mS/m)
0.10
0.15
0.20
0.25
2.0
2.5
3.0
3.5
SSA (m²/g)
RS
ALV (< 4 mm)
(b)
σ" (mS/m)
0.10
0.15
0.20
0.25
1.5
2.0
2.5
3.0
3.5
4.0
CEC (meq/100 g)
RS
ALV (< 4 mm)

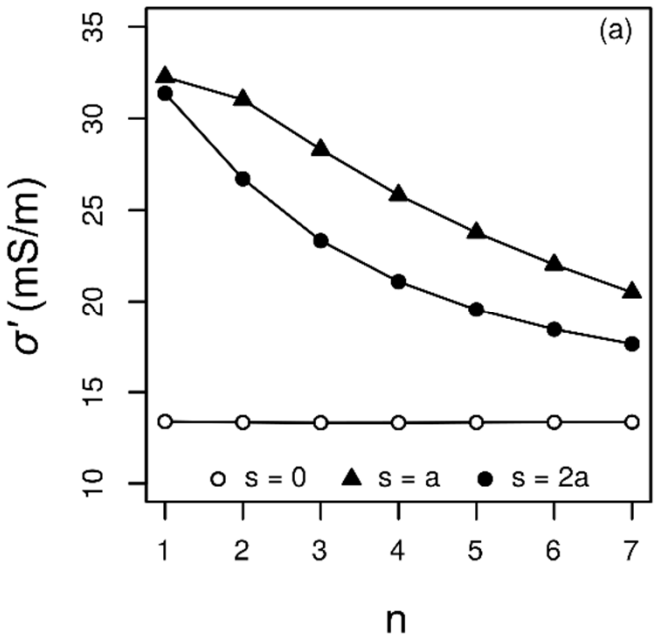
(a)
σ′ (mS/m)
10
15
20
25
30
35
1
2
3
4
5
6
7
n
s = 0
s = a
s = 2a

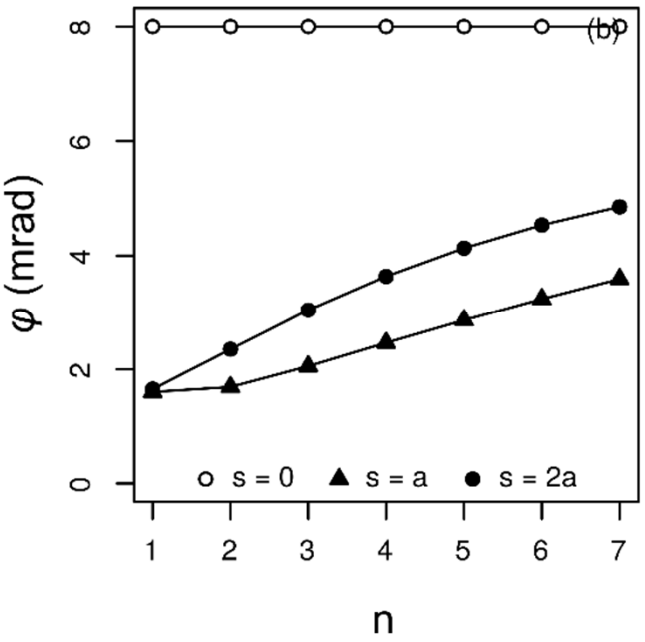
(b)
φ (mrad)
0
2
4
6
8
1
2
3
4
5
6
7
n
s = 0
s = a
s = 2a

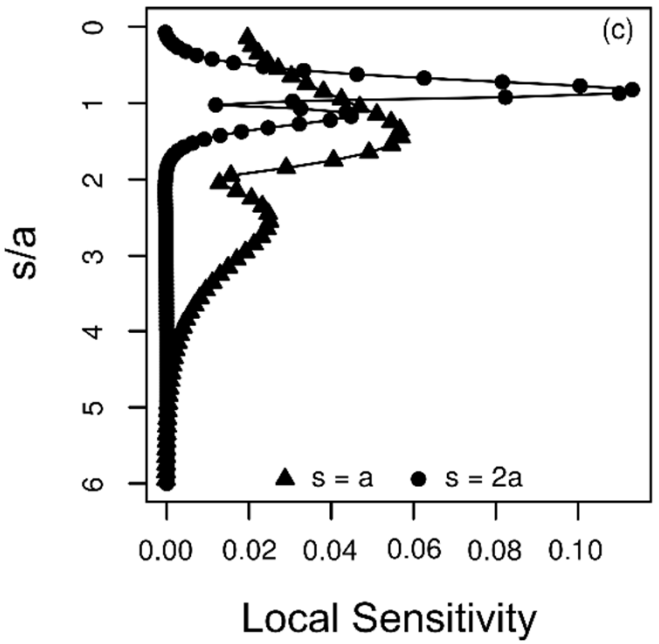
(c)
s/a
0
1
2
3
4
5
6
0.00
0.02
0.04
0.06
0.08
0.10
Local Sensitivity
s = a
s = 2a

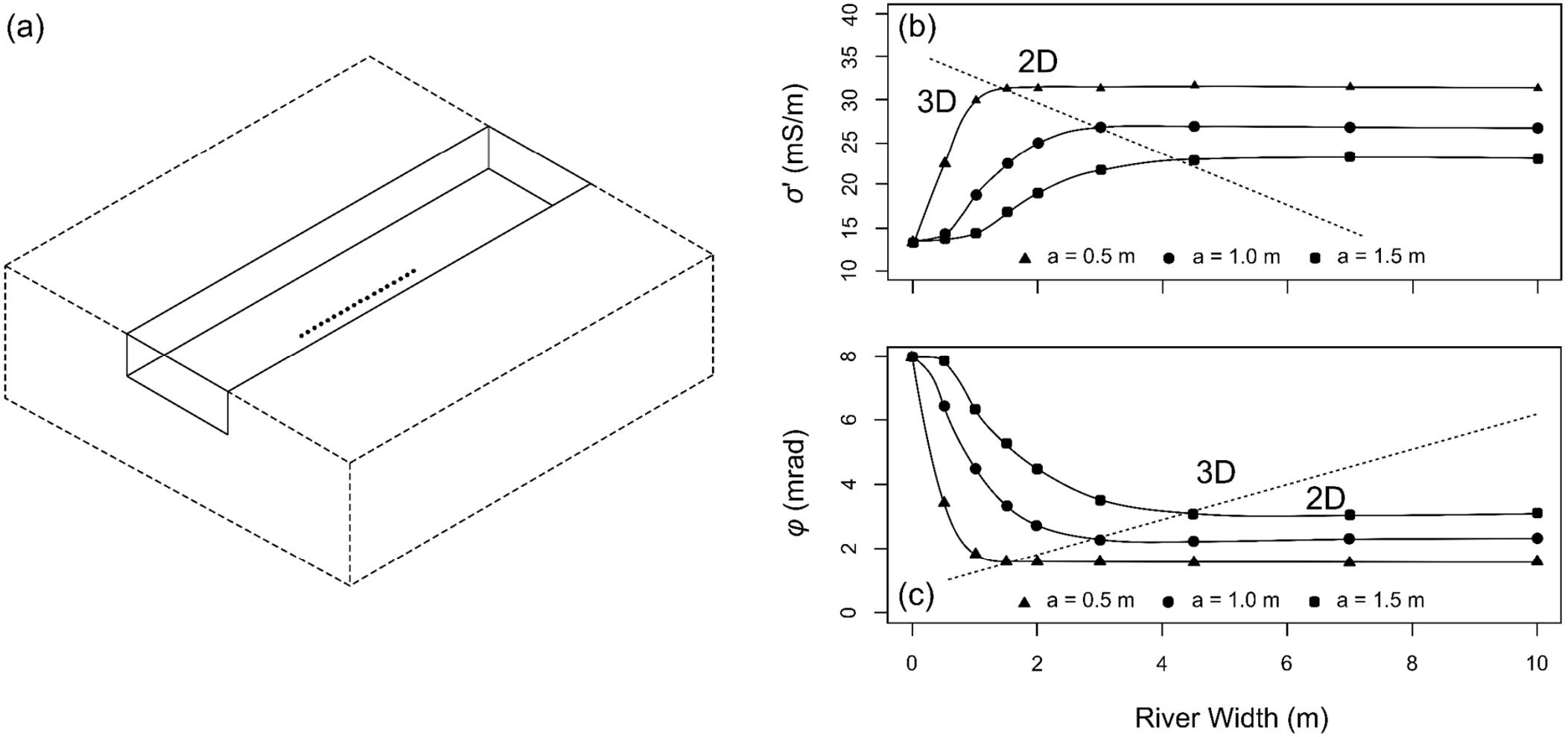
(a)
(b)
2D
3D
σ' (mS/m)
10
15
20
25
30
35
40
a = 0.5 m
a = 1.0 m
a = 1.5 m
(c)
3D
2D
φ (mrad)
0
2
4
6
8
0
2
4
6
8
10
River Width (m)

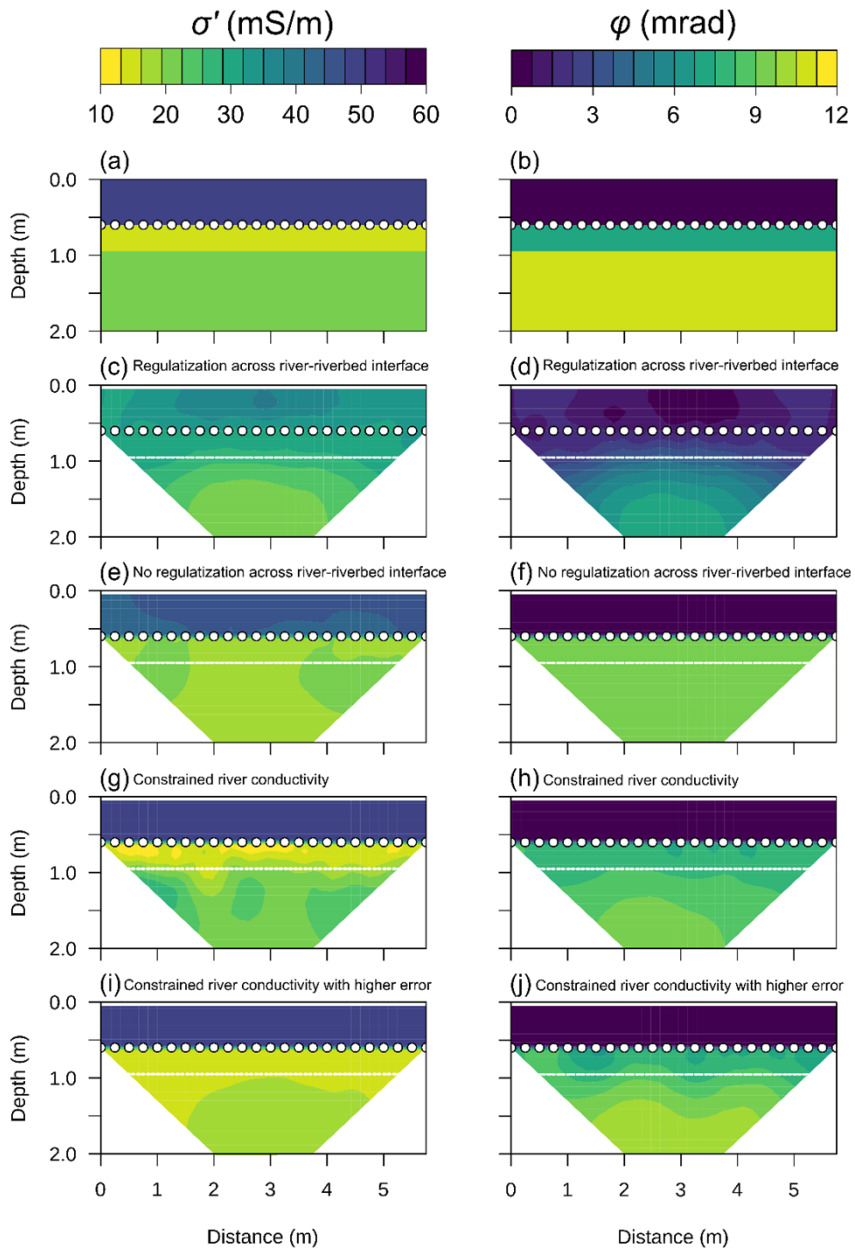
σ′ (mS/m)
10 20 30 40 50 60
φ (mrad)
0 3 6 9 12
(a)
(b)
(c) Regulatization across river-riverbed interface
(d) Regulatization across river-riverbed interface
(e) No regulatization across river-riverbed interface
(f) No regulatization across river-riverbed interface
(g) Constrained river conductivity
(h) Constrained river conductivity
(i) Constrained river conductivity with higher error
(j) Constrained river conductivity with higher error
Depth (m)
0.0
1.0
2.0
0 1 2 3 4 5
Distance (m)

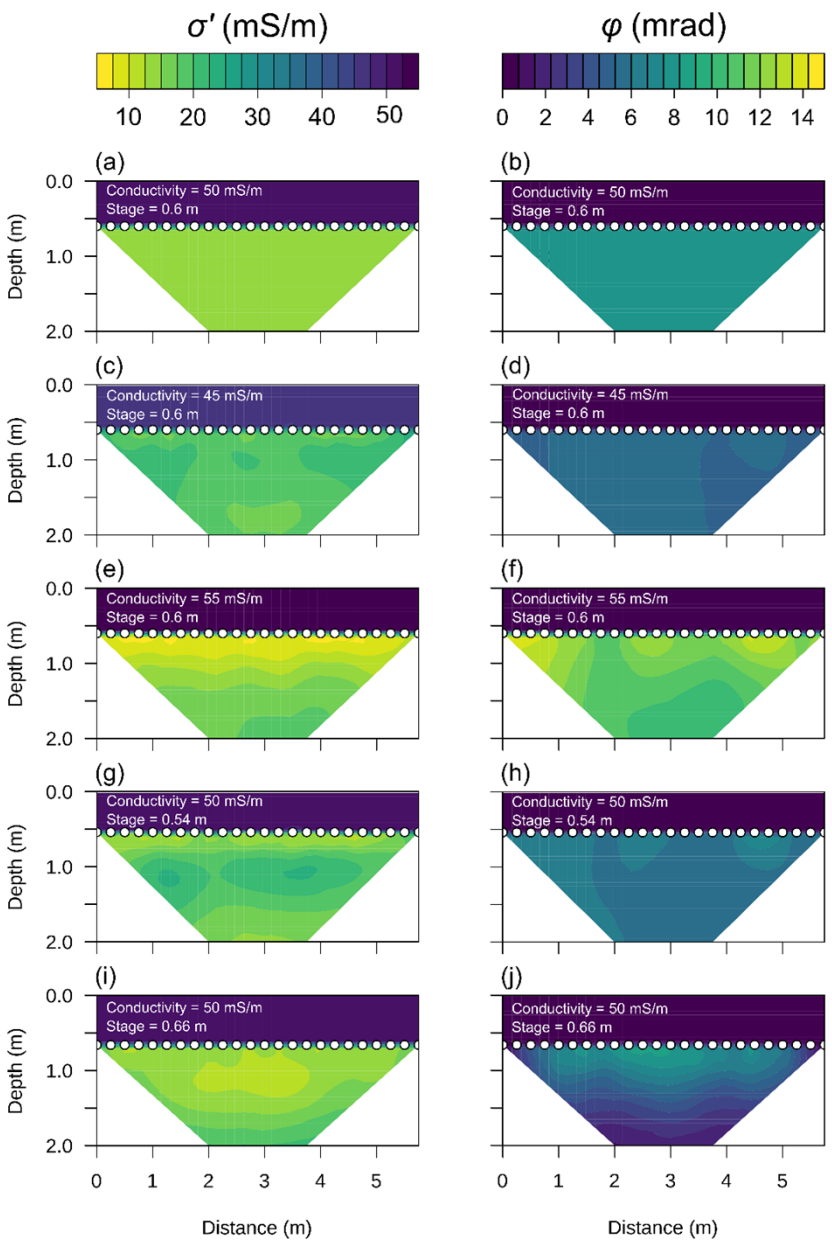
σ′ (mS/m)
10 20 30 40 50
φ (mrad)
0 2 4 6 8 10 12 14
(a)
Conductivity = 50 mS/m
Stage = 0.6 m
(b)
Conductivity = 50 mS/m
Stage = 0.6 m
(c)
Conductivity = 45 mS/m
Stage = 0.6 m
(d)
Conductivity = 45 mS/m
Stage = 0.6 m
(e)
Conductivity = 55 mS/m
Stage = 0.6 m
(f)
Conductivity = 55 mS/m
Stage = 0.6 m
(g)
Conductivity = 50 mS/m
Stage = 0.54 m
(h)
Conductivity = 50 mS/m
Stage = 0.54 m
(i)
Conductivity = 50 mS/m
Stage = 0.66 m
(j)
Conductivity = 50 mS/m
Stage = 0.66 m
Depth (m)
0.0
1.0
2.0
0 1 2 3 4 5
Distance (m)

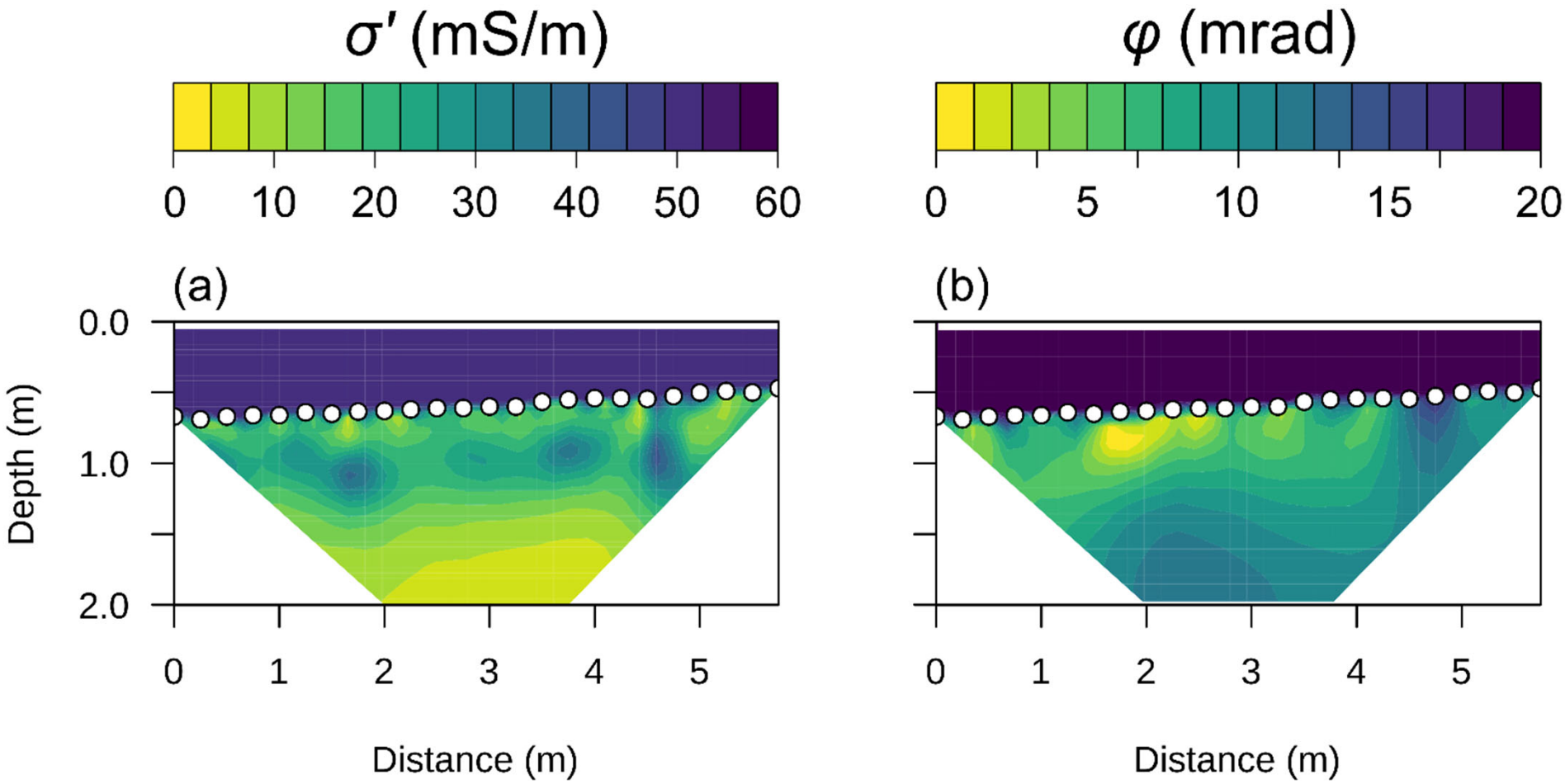
σ′ (mS/m)
0
10
20
30
40
50
60
φ (mrad)
0
5
10
15
20
(a)
(b)
Depth (m)
0.0
1.0
2.0
0
1
2
3
4
5
Distance (m)
Distance (m)

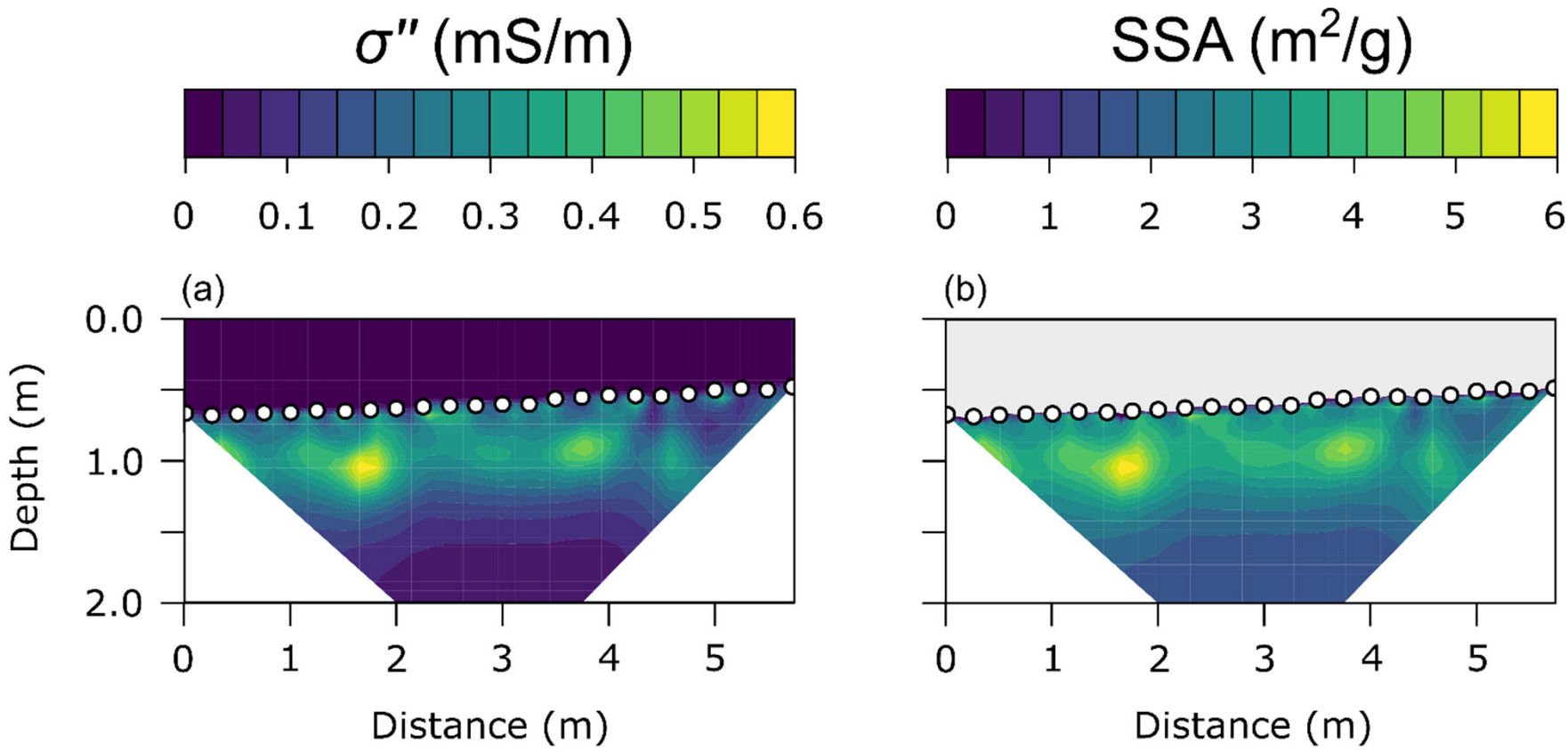
σ″ (mS/m)
0
0.1
0.2
0.3
0.4
0.5
0.6
SSA (m²/g)
0
1
2
3
4
5
6
(a)
(b)
Depth (m)
0.0
1.0
2.0
0
1
2
3
4
5
Distance (m)
Distance (m)